Biomedicine & Pharmacotherapy 193 (2025) 118855

Contents lists available at ScienceDirect

Biomedicine & Pharmacotherapy

journal homepage: www.elsevier.com/locate/biopha

Temporal and demographic patterns of peripheral nerve proteomes in preclinical neuropathic pain

Sabrina Grundtner [a], Feng Xian [a], Daniel Malzl [b,e], Tina Radits [a], Allison Marie Barry [a], Julia Regina Sondermann [a], Jörg Menche [b,c,d,e,f], David Gómez-Varela [a], Manuela Schmidt [a,*]

[a] Division of Pharmacology and Toxicology, Department of Pharmaceutical Sciences, University of Vienna, Vienna, Austria
[b] CeMM Research Center for Molecular Medicine of the Austrian Academy of Sciences, Vienna, Austria
[c] Max Perutz Labs, Vienna Biocenter Campus (VBC), Vienna, Austria
[d] Department of Structural and Computational Biology, Center for Molecular Biology, University of Vienna, Vienna, Austria
[e] Ludwig Boltzmann Institute for Network Medicine at the University of Vienna, Vienna, Austria
[f] Faculty of Mathematics, University of Vienna, Vienna, Austria

ARTICLE INFO

Keywords:
neuropathic pain
sciatic nerve
unbiased proteomics
MEFISTO
sex
age
protein networks
nerve injury
chronic pain
longitudinal profiling
mouse

ABSTRACT

Peripheral nerves drive movement and sensation but are highly vulnerable to injury, making them critical sites in the development of neuropathic pain. Nerve trauma initiates profound plasticity, yet the molecular programs driving both early and persistent axonal remodeling remain poorly understood. Here, we present a uniquely longitudinal proteomic perspective on injured sciatic nerve fibers, spanning acute (7–14 days) to chronic (98 days) stages in the mouse spared nerve injury (SNI)-model of neuropathic pain. Given the importance of demographic diversity in pain research, we compared male and female mice at adolescent and adult stages. Using MEFISTO (MEssage FInding for Spatio-Temporal Ordering), a time-aware latent factor model, we resolved complex proteome trajectories and identified temporal patterns of injury-induced axonal reorganization. Notably, we observed sex- and age-biased differences in immune and neuronal pathways. Despite comparable pain behaviors, these molecular distinctions suggest heterogeneity of nerve injury-induced molecular changes. In parallel, a robust sex-shared injury response emerged, characterized by early neuronal injury/repair, sustained metabolic and immune reprogramming and late structural and transcriptional remodeling. Many dozens of identified proteome alterations match transcriptome changes in nerves from human patients with neuropathy highlighting the translational relevance of our data. In summary, we provide a demographically inclusive, temporally resolved resource that advances our understanding of long-term peripheral nerve remodeling. By bridging early and late injury phases our findings provide a framework for mechanistic translational research and identifying therapeutic targets relevant to nerve injury and associated neuropathic pain.

1. Introduction

The transition from acute to chronic pain is a critical biomedical problem with profound implications for patient care and therapeutic development. Peripheral nerve injury is one of the major drivers of this transition, initiating complex, temporally dynamic, and compartment-specific responses across the peripheral nervous system. While dorsal root ganglia (DRG), the site of sensory neuron somata, have been extensively profiled using transcriptomic and proteomic approaches [1–4], less is known about the molecular remodeling that occurs in

Abbreviations: DRG, Dorsal root ganglia; SNI, Spared nerve injury; DEPs, Differentially expressed proteins; FDA, Food and Drug Administration; MEFISTO, MEssage FInding for Spatio-Temporal Ordering; MOFA, Multiomics factor analysis; MS, Mass spectrometry; PBS, Phosphate-buffered saline; DTT, Dithiothreitol; SDS, Sodium dodecyl sulfate; IAA, Iodoacetamide; SP3, Single-pot, solid-phase-enhanced sample preparation; ACN, Acetonitrile; FA, Formic acid; LC-MS, Liquid chromatography-mass spectrometry; DIA, Data-independent acquisition; PASEF, Parallel accumulation-serial fragmentation; PPI, Protein-protein interaction; GO, Gene Ontology; STable, Supplementary table; Cacna2d1, Calcium voltage-gated channel auxiliary subunit alpha2delta 1; Trpv1, Transient receptor potential vanilloid channel 1; Scn channels, Sodium voltage-gated channels; Kcnab2, Potassium voltage-gated channel subfamily A regulatory beta subunit 2; Kcnb2, Potassium voltage-gated channel subfamily B member 2.

* Corresponding author.
E-mail address: manuela_schmidt@univie.ac.at (M. Schmidt).

https://doi.org/10.1016/j.biopha.2025.118855
Received 18 September 2025; Received in revised form 12 November 2025; Accepted 30 November 2025
Available online 4 December 2025

peripheral nerve fibers themselves. This represents a major gap: the sciatic nerve is not only a structural conduit for sensory input and motor output but also a key site of Wallerian degeneration [5], demyelination, immune cell infiltration, and regenerative activity following nerve injury [6–8]. Moreover, it provides the anatomical substrate for widely used preclinical neuropathic pain models, including the spared nerve injury (SNI) model [9].

Emerging work highlights the importance of considering demographic variables such as sex and age in pain research [10,11]. In the context of chronic pain, such differences may critically influence susceptibility, recovery, and therapeutic response. Most studies have focused on uncovering how age and sex intersect with pain-relevant signaling pathways in DRG [3,4,12,13], however, injured axons of peripheral nerves have only been marginally assessed. We have recently applied our workflow for deep proteome profiling in naïve sciatic nerves and revealed profound sex- and age-dependent baseline signatures, underscoring that demographic heterogeneity shapes the molecular landscape of the peripheral nervous system [14].

Here, we characterize proteome dynamics of the sciatic nerve after SNI in male and female mice at adolescent and adult age. Unlike most prior molecular studies, which focus on early to mid-range phases (0–28 days), our analysis spans both early (day 7–14) and late (day 98) time points, enabling us to capture long-term remodeling events associated with nerve injury and, potentially, neuropathic pain. Our data reveal distinct sex-biased and age-modulated proteomic trajectories, alongside a shared core response to nerve injury that is conserved across sex. This includes changes in immune and inflammatory processes, neuroplasticity, metabolic pathways, and long-term structural as well as transcriptional remodeling — processes implicated in sustaining maladaptive pain states.

Taken together, our findings provide an expansive, demographic-aware and temporally resolved resource for understanding peripheral nerve injury and triggers for neuropathic pain. Importantly, our study underscores the translational value of inclusive experimental designs that integrate sex, age, and chronicity as key biological variables in mechanistic translational research on nerve injury and associated neuropathic pain.

2. Materials and methods

Key Resources Table

Reagent type (species) or resource	Designation	Source or reference	Identifiers	Additional information
Mouse strain	C57BL/6 J	In house bred		Wild type, female and male, 4 and 12 weeks old
Chemical compound	Isoflurane	Cp-pharma	Ch.B.: G135K21A	
Chemical compound	Carprofen	Zoetis	Ch.B.: 2026885	
Chemical compound	Sodium Chloride	Fresenius Kabi	Ch.B.: 20SIF002	
Chemical compound	Bepanthen	Bayer Austria	/	
Chemical compound	Octenisept	Schülke & Mayr	Ch.B.: 1586155	
Chemical compound	Povidone-iodine	B. Braun Melsungen	Ch.B.: 15234M15	
Chemical compound	Tris 1 M	Lonza	51237	
Chemical compound	Glycerol	Fisher Scientific	10021083	
Chemical compound	Dithiothreitol 1 M	Sigma-Aldrich	43816	
Chemical compound	Sodium dodecyl sulfate	Fisher Scientific	10625405	
Chemical compound	Acetone	Sigma-Aldrich	1000201000	
Chemical compound	Ethanol	Sigma-Aldrich	1117272500	
Chemical compound	Iodoacetamide	Sigma-Aldrich	I1149	
Chemical compound	Sera-Mag SpeedBead beads	Cytiva	65152105050250, 1:1 mix 45152105050250	
Chemical compound	Ammonium bicarbonate	Sigma-Aldrich	09830–500 G	
Chemical compound	Trypsin/Lys-C	Promega	V5073	
Chemical compound	Acetonitrile	Fisher Scientific	10001334	
Chemical compound	Water MS grade	Sigma-Aldrich	1153331000	
Chemical compound	Formic Acid	Fisher Scientific	15658430	
other	Surgical silk	Vömel	Ch.B.: 001367	
other	AutoClip Applier	Mikron Precision	205000	
other	AutoClip Remover	Mikron Precision	205009	
other	Surgical clip	Fine Science Tools	205016	
other	Protein LoBind tube	Eppendorf	0030108116	Reagent tube
other	Complete protease inhibitor cocktail	Roche/ Merck	58929700001	Mix of protease inhibitors
software, algorithm	ImageJ Fiji	https://imagej.net/software/fiji/		Version 1.53k
software, algorithm	GraphPad Prism	https://www.graphpad.com/		Version 8.0
software, algorithm	DIA-NN	https://github.com/vdemichev/DiaNN		Version 1.9
software, algorithm	R	https://www.r-project.org/		Version 4.3.2
software, algorithm	MEFISTO	https://github.com/menchelab/Grundtner_et_al_2025		
software, algorithm	MOFA – muon package	https://github.com/scverse/muon		
software, algorithm	Cytoscape	https://cytoscape.org/download.html		Version 3.10.1
software, algorithm	ClueGO	https://apps.cytoscape.org/apps/cluego		Version 2.5.10
software, algorithm	STRING	https://string-db.org/		Version 12.0

(continued on next column)

(continued)

(continued on next page)

(*continued*)

Key Resources Table		
software, algorithm	Seurat	https://satijalab.org/seurat/

2.1. Experimental mice

Animal handling and housing conditions followed previously published procedures [4,14]. In brief, wildtype C57BL/6 J mice were purchased (Charles River Laboratories, Massachusetts, USA) and bred in-house. Mice were group-housed (2–4 mice per cage) according to sex, age, time point and experimental condition (SNI, Sham, Naïve), in open housing cages, with a 12 h light/dark cycle and water and food *ad libitum*. Male and female mice of two age groups (adolescent, i.e., 4 weeks at nerve injury, and adult, i.e., 12 weeks at nerve injury) were used for this study as in our prior work [14]. Experimental cohorts were defined based on their day of sacrifice (day (D) 7, D14, and D98 post nerve injury). Naïve non-treated mice were used as additional controls for proteome data analysis on D7 and D98. Of note, sampling and analysis started at D7 due to our animal licence. Each cohort consisted of 5–6 mice. For behavior analysis, data from multiple cohorts were pooled, resulting in high replicate numbers (up to $n = 35$). Mouse handling (operation, weighing, behavioral experiments and sacrifice) was conducted by female experimenters, in line with findings from Sorge *et al.* [15]. All animal experiments were approved by the IACUC at the University of Vienna and the Austrian Ministry for Education, Science and Research (BMBWF; license number 2021–0.138.925). International ARRIVE guidelines [16] and the EU recommendations (Directive 2010/63/EU) for studies on animals were followed.

2.2. Spared nerve injury (SNI) model of neuropathic pain

Neuropathic pain was induced using the spared nerve injury (SNI) model [9,17], and essentially as previously described [4,18]. Briefly, mice were anesthetized with isoflurane (cp-pharma, Burgdorf, Germany). Carprofen (Rimadyl, Zoetis, New Jersey, USA) was injected subcutaneously for analgesia (0.05 mL/10 g body weight diluted 1:25 with 0.9 % NaCl). To prevent corneal dehydration during surgery, eyes were covered with eye ointment (Bepanthen Augen- und Nasensalbe, Bayer Austria Ges.m.b.H., Vienna, Austria). The surgical area was disinfected with Octenisept (Schülke & Mayr GmbH, Norderstedt, Germany). A skin incision and blunt dissection of the *biceps femoris* muscle on the left side was done to expose the trifurcation of the sciatic nerve. The two branches of the sciatic nerve, the common peroneal and tibial nerves, were ligated using a non-resorbable, braided, 7–0 silk (Vömel, Kronberg, Germany) and then transected distal to the ligation. To prevent nerve regeneration, a 2 mm nerve segment was excised. The surgical wound of the skin was closed with a surgical clip (Fine Science Tools, Heidelberg, Germany), using the AutoClip Applier (Mikron Precision Inc, California, USA) and the surgery site was disinfected with povidone-iodine solution (Braunol®, B. Braun Melsungen AG, Melsungen, Germany). On day 1 (D1) post-injury, postoperative analgesia was administered with carprofen (0.05 mL/10 g body weight diluted 1:25 with 0.9 % NaCl). On D5 post-injury, surgical clips were removed using the AutoClip Remover (Mikron Precision Inc). Sham-operated mice, which served as control group, underwent the identical surgical procedure, including anaesthesia, analgesia, eye ointment and disinfection but without nerve ligation and transection. Body weight of operated mice was monitored daily until D7, every other day until D14, every fourth day until D28, and once a week until D98 post-injury. No adverse events or abnormal bleeding were observed during surgery or recovery across experimental groups. Naïve, untreated mice served as additional controls for proteomic analysis. All mice were randomly assigned to the experimental groups (SNI, Sham, or Naïve).

2.3. Mouse behavior

Behavioral assays were conducted on SNI and Sham-operated mice, between 8:00 am and 3:00 pm, by female experimenters only. Experimenters were officially blinded to experimental condition, sex and age, but complete blinding was not feasible due to visible characteristics such as body size, sex-specific physical characteristics, sutures at the surgical site, or altered gait due to nerve injury. All procedures were conducted as described previously [4].

Paw print area (Non-evoked pain)

Non-evoked pain (NEP)-related behavior was assessed using a video-based approach as described in Pogatzki-Zahn *et al.* [19]. In brief, mice were placed individually on a 1 cm thick Plexiglas plate, surrounded by green light emitting diodes (LEDs), and enclosed in transparent plastic boxes (9.5 ×9.5 cm) atop a red LED plate. Ventral recordings were used to capture the paw print of the mice for 10 min, in a dark room, from a distance of 30 cm, using a portable camera (Hero 8 Black, GoPro, California, USA; settings: 1080p, 60 frames, linear), without experimenters being present. From each video, 10 randomly selected frames were analyzed using ImageJ Fiji [20] to determine the mean paw print area. Frames were included only if both hind paws were clearly visible, the animal was not rearing, and no excessive urination obstructed the view. In addition, mice were excluded from the analysis at specific time points if less than 10 suitable frames could be obtained. Paw print data were expressed as the ratio of ipsilateral (injury side; left) to contralateral (non-injury side; right) paw area, normalizing for potential body weight effects. Two experimenters independently analyzed the frames to ensure consistency.

The number of mice per group was as follows:

Sham:

-Pre: 4w (male: 35, female 32), 12w (male: 31, female: 27)

-D7: 4w (male: 34, female 32), 12w (male: 26, female: 27)

-D14: 4w (male: 18, female 18), 12w (male: 19, female: 11)

-D98: 4w (male: 11, female 12), 12w (male: 6, female: 6)

SNI:

-Pre: 4w (male: 32, female 32), 12w (male: 32, female: 29)

-D7: 4w (male: 31, female 32), 12w (male: 31, female: 29)

-D14: 4w (male: 18, female 18), 12w (male: 20, female: 12)

-D98: 4w (male: 9, female 12), 12w (male: 6, female: 6)

Mechanical stimulation (Evoked pain)

Mechanical hypersensitivity was assessed using the Dynamic Plantar Aesthesiometer (37450–001, Dynamic Plantar Aesthesiometer Touch Stimulator: 37400–002, Ugo Basile®, Gemonio, Italy) as described previously by Gómez-Varela *et al.* [4,18]. Briefly, in the week prior to baseline testing (Pre), mice were habituated to the testing grid (5 ×5 mm square holes) for 4 h. Behavioral testing was performed after a 2 h acclimatization period on the testing grid on D7, D14, and D98. Paw withdrawal thresholds (PWTs) were recorded as the latency (in seconds) in response to a mechanical stimulus (Force Intensity: 10 g; Ramp Time: 40 s) applied to the lateral plantar surface of each hind paw. Each hind paw was tested five times per session, with a minimum 2 min recovery between each measurement. Mice were excluded from the respective time point if less than three measurements per hind paw could be obtained. PWTs were calculated as the ratio of ipsilateral (injury side; left) to contralateral (non-injury side; right) hind paw responses.

The number of mice per group was as follows:

Sham:

-Pre: 4w (male: 12, female 12), 12w (male: 11, female: 11)

-D7: 4w (male: 12, female 12), 12w (male: 11, female: 11)

-D14: 4w (male: 12, female 12), 12w (male: 11, female: 11)

-D98: 4w (male: 11, female 12), 12w (male: 11, female: 10)

SNI:

-Pre: 4w (male: 12, female 12), 12w (male: 12, female: 12)

-D7: 4w (male: 12, female 12), 12w (male: 12, female: 12)

-D14: 4w (male: 12, female 9), 12w (male: 12, female: 10)
-D98: 4w (male: 11, female 12), 12w (male: 12, female: 12)

2.4. Statistical analysis

GraphPad Prism 8.0 (California, USA) was used to analyze behavioral data. Mixed-effects analysis with Holm-Šídák multiple comparison correction was used. Data is depicted as median ± interquartile range. All replicates are biological replicates. Adjusted *p*-value: * 0.0055, ** 0.0001, *** < 0.0001.

2.5. Isolation of sciatic nerve (SCN)

Mice were randomly assigned into three different cohorts, depending on the day of sacrifice (D7, D14, and D98 post-injury). After euthanization with CO_2, the sciatic nerve was collected by cutting open the skin of the leg and the underlying *biceps femoris* muscle, exposing the sciatic nerve. 1 cm of the sciatic nerve of the ipsilateral side (injury-side; left) was collected proximal to distal until the bifurcation using Fine Science Tools (FST, Heidelberg, Germany) and Dumont (Montignez, Swiss). The isolated sciatic nerve was flash-frozen in liquid nitrogen and stored at −80°C until further use. Each sample corresponds to one mouse, with one sciatic nerve (ipsilateral) collected per animal.

The number of mice per group was as follows:
Naïve:
-D7: 4w (male: 6, female 6), 12w (male: 6, female: 6)
-D14: NA
-D98: 4w (male: 3, female 3), 12w (male: 3, female: 3)
Sham:
-D7: 4w (male: 6, female 6), 12w (male: 6, female: 6)
-D14: 4w (male: 6, female 5), 12w (male: 5, female: 6)
-D98: 4w (male: 6, female 6), 12w (male: 6, female: 6)
SNI:
-D7: 4w (male: 6, female 6), 12w (male: 6, female: 6)
-D14: 4w (male: 6, female 6), 12w (male: 6, female: 5)
-D98: 4w (male: 5, female 6), 12w (male: 6, female: 6)

2.6. Protein extraction

Protein extraction was performed following closely the protocol described in our original study [14]. In brief, SCN tissue was transferred into 250 µL of lysis buffer in protein LoBind tubes (Eppendorf, Hamburg, Germany) containing 100 mM Tris–HCl, 5 % glycerol, 10 mM dithiothreitol (DTT), 2 % sodium dodecyl sulfate (SDS), 1x cOmplete Protease Inhibitor Cocktail (Roche, Basel, Switzerland). Samples were sonicated using a Bioruptor Pico (Diagenode, Seraing, Belgium) for 10 cycles (30 s on and 30 s off) at 4°C, low frequency. Following sonication, samples were incubated at 70°C for 10 min with agitation at 1500 rpm. Tissue debris was removed by centrifugation at 10,000 x g for 5 min. After transferring the supernatant to a new protein LoBind tube, lipids were precipitated by adding 5 volumes of ice-cold acetone and incubating at -20°C for 4 h. Acetone was removed and protein pellets recovered by centrifugation at 14,000 x g for 30 min, followed by washing with ice-cold 80 % ethanol (v/v), and another round of centrifugation under the same conditions. Pellets were air-dried at room temperature for 30 min. The dried protein pellet was reconstituted in 50 µL lysis buffer and incubated at 60°C for 10 min with agitation (1500 rpm). After brief centrifugation (14,000 x g, 1 min), protein concentration was measured at 280 nm, using a NanoPhotometer N60 (Implen GmbH, München, Germany). For downstream processing, 50 µg of protein was diluted to a volume of 90 µL with lysis buffer. Samples were sonicated (Bioruptor Pico, 30 s on and 30 s off, 4°C, low frequency). Proteins were reduced with 5 mM DTT for 30 min at 60°C with agitation (1000 rpm), followed by alkylation with 20 mM iodoacetamide (IAA) for 30 min at room temperature in the dark. Excess IAA was quenched by adding 5 mM DTT for 15 min at room temperature.

2.7. SP3-assisted protein digestion

Single-pot, solid-phase-enhanced sample preparation (SP3) was carried out as described in our original study [14] adapted from Hughes *et al.* [21]. Briefly, 10 µL of pre-mixed Sera-Mag SpeedBead beads (Cytiva, Marlborough, MA) were used per 50 µg of total protein. Protein binding was initiated by adding one volume of absolute ethanol. Samples were incubated for 5 min at 24°C with agitation (1000 rpm) on a Thermomixer (Eppendorf), followed by a 2 min incubation on a magnetic rack (DynaMag™-2 Magnet, Invitrogen by ThermoFisherScientific, Waltham, USA). The supernatant was discarded, and beads were washed three times with 400 µL of 80 % ethanol (v/v). Beads were resuspended in 50 µL of digestion buffer (50 mM ammonium bicarbonate, pH 8) and proteins were digested overnight (18 h) at 37°C with agitation (950 rpm) using 2 µg of trypsin/Lys-C. Following digestion, 100 % acetonitrile (ACN), to a final concentration of 95 %, was added and incubated for 10 min at room temperature, whereby the last 2 min incubation was done on a magnetic rack. The supernatant was discarded and beads were rinsed with ACN to a final concentration of 100 % and incubated again on a magnetic rack for 2 min. The remaining solvent was removed and beads were air-dried for 1 min. Peptides were eluted in 20 µL LC-MS grade water and peptide concentration was measured at 205 nm, using a NanoPhotometer N60 (Implen). Before samples were stored at −20°C, samples were acidified with formic acid (FA) to a final concentration of 0.1 %.

2.8. LC-MS/MS setup

Mass spectrometry was performed following the protocol described in our original study [14]. In brief, nanoflow reversed-phase liquid chromatography (Nano-RPLC) was conducted using a NanoElute2 system (Bruker Daltonik, Bremen, Germany). A total of 250 ng of digested peptides were injected and separated on a 25 cm × 75 µm column, packed with 1.6 µm C18 particles (IonOpticks, Fitzroy, Australia), using a 60 min gradient. Mobile phase A consisted of 100 % water (LC-MS grade) with 0.1 % FA, while mobile phase B was 100 % ACN with 0.1 % FA. The separation was performed at a flow rate of 250 nL/min, except for the final 7 min, during which the flow rate was increased to 400 nL/min. The gradients included a linear increase of mobile phase B from 4 % to 20 % over the first 35 min, followed by an increase to 35 % over 17 min. Subsequently, mobile phase B was ramped up to 85 % within 0.5 min and held at this level for 7 min to elute hydrophobic peptides. Peptide eluates were analyzed on a hybrid TIMS quadrupole TOF mass spectrometer (timsTOF HT, Bruker Daltonik) coupled via a CaptiveSpray ion source. Data acquisition was performed in data-independent acquisition (DIA) mode, in combination with parallel accumulation serial fragmentation (PASEF). The TIMS analyzer operated at 100 % duty cycle with an accumulation and ramp time of 100 ms. Ion mobility separation was set in the range of 0.65–1.35 (1/k0). Precursors within an m/z range of 350–1150 were targeted in 13 scan cycles, comprising 32 isolation windows of 25 Th, resulting in a total cycle time of 1.48 s. Collision energy was ramped linearly from 65 eV at $1/k0 = 1.6$–20 eV at $1/k0 = 0.6$.

2.9. DIA-PASEF data processing

To process DIA-PASEF data DIA-NN (version 1.9) was used in library-free mode and based on the *M. musculus* proteome database as described in our original study [14]. Within DIA-NN, a deep learning-based method was used to predict theoretical peptide spectra, retention time, and ion mobility. Trypsin/P was used for *in silico* digestion, with a maximum of 2 missed cleavage. Peptide identification allowed up to two variable modifications per peptide, including methionine oxidation and N-terminal acetylation. Carbamidomethylation on cysteine was selected as a fixed modification. Peptides were restricted to lengths between 7 and 30 amino acids. The m/z range was defined according to the

DIA-PASEF acquisition method: 350–1150 for precursor ions and 100–1700 for fragment ions. Mass accuracy for both MS1 and MS2 was set to automatic determination. Protein inference was performed at the gene level, with the "Heuristic protein inference" option disabled. Cross-run matching was enabled using the match-between-runs (MBR) feature. Quantification was carried out using retention time–dependent cross-run normalization with the "QuantUMS (high precision)" setting. Additional processing of the DIA-NN search results was carried out using the R [22] package DIA-NN (https://github.com/vdemichev/diann-rpackage), with a quantitative intensity extraction for all identified peptides and protein groups (a q-value of ≤ 0.01 was set at precursor and protein group level).

2.10. Differential expression analysis

10312 protein groups were quantified. For differential expression analysis (SNI – Sham), protein groups were retained if they were quantified in at least 75 % of replicates within each experimental condition (male/female, adolescent/adult and time points). Quantitative protein data were imported into the R package ProTIGY (https://github.com/broadinstitute/protigy), and $\log_2$-transformed. Statistical significance (SNI – Sham) was assessed using two-sample moderated t-test. Contrasts were stratified by sex (F = female, M = male), age (4w = adolescent, 12w = adult) and time point (D7, D14, D98). In each contrast, proteins were considered differentially expressed (DEPs) with an adjusted (Benjamini and Hochberg, for multiple testing) p-value ≤ 0.05 (hereafter referred to as the q-value). For all DEP comparisons, the first mapped protein of each protein group was used for annotation.

2.11. Factor analysis with MEFISTO

Multiomics factor analysis (MOFA) (Bioconductor package MOFA2) [23] was similarly done as described previously [4]. We used MEssage FInding for Spatio-Temporal Ordering (MEFISTO) [24], an extension of the MOFA framework, and the muon package (https://github.com/scverse/muon), a Python framework for multiomics data, which allows usage of MEFISTO. Since MEFISTO algorithm, similar to other modern machine learning methods, benefits in the input dataset from a high number of features (i.e., quantified proteins), we included data from naïve mice in this analysis. Furthermore, not all input characteristics are necessarily informative, i.e., some may not contain information about differences or similarity between our experimental groups. Potential noise and missing values were removed by filtering out proteins with a missing value higher than 50 % in any time x condition group. Of note, we did not use the MEFISTO option to impute missing data. After filtering for missing values, we retained 6654 proteins. The $\log(x+1)$ transformed and filtered data was then used to fit a 50-factor MEFISTO model. We employed the 50-factor MEFISTO model as the variance explained by our main metadata features was relatively subtle and not adequately captured by the default 10-factor model. In brief, we reformatted the transformed and filtered data into an AnnData object using anndata v0.8.0 and subsequently used the MOFApy2 (v0.6.7) interface of muon v0.1.2 to fit MEFISTO with n_factors = 50, groups_label = 'condition', center_groups = False, n_iterations = 2000, smooth_covariate = 'timefactor', smooth_kwargs = {"n_grid": 50, "start_opt": 50, "opt_freq": 50}, seed = 2023, convergence_mode = 'fast'. We annotated the resulting factors by performing overrepresentation analysis in GO Biological Processes 2025 through the Enricher API of gseapy (https://doi.org/10.1093/bioinformatics/btac757). We computed associated and antiassociated terms by ranking the proteins by their factor weight and then taking the top / bottom 2.5 % to feed into Enrichr. Code used for MEFISTO analysis was deposited at Zenodo under the following DOI: 10.5281/zenodo.16737895 (https://github.com/menchelab/Grundtner_et_al_2025). The computational results presented were obtained using the LiSC cluster (https://lisc.univie.ac.at/).

2.12. Pathway analysis

Pathway analysis of DEPs was done using Cytoscape [25] and the ClueGO app [26], with GO – Biological Processes (GO-BP) as Ontologies/Pathways. Species was set to *Mus musculus*. Medium network specificity was selected. GO Term fusion was applied and only pathways were included with a $p \leq 0.05$. For the GO Term/Pathway Network Connectivity (Kappa Score) a score of 0.5 (medium) was used. Remaining pathway options were left as default. Enrichment/Depletion (Two-sided hypergeometric test) and Benjamini-Hochberg were used. Grouping options were set as default.

Pathway analysis of DEPs and sex-shared DEPs was done using Cytoscape (v3.10.1) [25], ClueGO app (v2.5.10) [26] and Ontologies/-Pathways (updated May 2024). Pathway analysis of sex-enriched DEPs was done using Cytoscape (v3.10.4) [25], ClueGO app (v2.5.10) [26] and Ontologies/Pathways (updated November 2025).

2.13. Protein-protein interaction network

The protein-protein interaction (PPI) networks were done using STRING (v12.0) [27] and Cytoscape (v3.10.1) [25]. Networks were generated using *Mus musculus* as species and with an interaction score of 0.7 (high confidence). For visualization purposes, single nodes not being connected within a network were removed. The PPI network of sex-shared DEPs was based on sex-shared DEPs from pathways overlapping (based on GO ID) from MEFISTO factor 22 & 31 and pathways from sex-shared DEPs. The PPI network of interferon (IFN) signaling was based on single protein input Ifit3 in STRING (v12.0) [27] with 50 interactors for 1st and 2nd shells.

2.14. Transcriptomic comparison to the injured sciatic nerve atlas (iSNAT)

Seurat objects for 0 and 7 days were accessed from the injured sciatic nerve atlas (iSNAT) (GEO: GSE198582) [28]. Count matrices for each object were converted to a reduced memory format using the BPCells package [29] prior to conversion from Seurat V3 to V5 objects [30]. Barcodes were integrated using CCA integration following a standard pipeline: Objects were merged, with layers joined for initial normalization. Layers were re-split by timepoint prior to scaling ('Seurat::ScaleData') and integration ('Seurat::IntegrateLayers(object, method = CCAIntegration, orig = "pca", new.reduction = "integrated.cca", dims = 1:30, k.anchor = 20)`). Data was clustered at a resolution of 0.5, and published cell type annotations from the iSNAT atlas were overlayed. Barcodes with missing cell type annotations were excluded, and layers were joined prior to downstream plotting.

Differentially expressed genes were calculated via `Seurat::FindMarkers` using a wilcox test after subsetting by cell type. Only genes expressed in 10 % of barcodes were included. Some cell types were only present at day 7 and not day 0, reflecting an infiltration into the nerve. Here, differentially expressed genes could not be calculated. Genes were considered significant with an FDR < 0.05, and an absolute LFC > 1. Cell type markers were calculated with `Seurat::FindAllMarkers`, with significance considered at an FDR < 0.05, and a positive LFC > 1. Overlapped gene symbols were then calculated against sex-dependent DEPs.

2.15. Use of generative AI

Generative AI tools (OpenAI ChatGPT) were used solely to improve phrasing, clarity, and formatting. All scientific concepts, experimental designs, hypotheses, and project goals were developed by the research team. No synthetic or AI-generated data were included.

3. Results

3.1. Overview of sciatic nerve proteomic profiling across sex, age, and injury time points

To characterize the protein signature of the sciatic nerve upon injury, we conducted deep proteome profiling in a mouse model of spared nerve injury (SNI) [9]. In accordance with our previous study [14] we analyzed pain-associated behaviors in male and female mice of two age groups (adolescent mice, 4 weeks at nerve injury, and adult mice, 12 weeks at nerve injury). The induction of neuropathic pain was confirmed by development of mechanical hypersensitivity (evoked pain; SFigure 1A-B) [9] and the decrease of the paw print area as a proxy for non-evoked pain (NEP; SFigure 1C-D) in all mice [19,31]. These pain-related behaviors were largely similar across sex and age groups and stable among analyzed time points as reported elsewhere [12,32,33]. Sciatic nerve tissue was isolated at distinct time points: early after injury at day (D) 7 and D14 and late after injury (D98) (Fig. 1A). The time points were chosen to cover the early and chronic phase after nerve injury [33] – the latter being underrepresented in published molecular studies. Sham injury served as control condition.

For deep proteome profiling, we performed mass spectrometry using data-independent acquisition with parallel accumulation serial fragmentation (DIA-PASEF) [34] (please see methods for details) enabling deep and comprehensive proteome profiling as shown in our earlier work on sciatic nerves [14]. We consistently (please see technical quality criteria in SFigure 2A-D and in methods) quantified a core set of $>$ 9000 proteins across all time points (SFigure 2E) and conditions (SNI, Sham, and Naïve controls) (Fig. 1B; STable 1). Given the robustness (SFigure 2A-D) and broad dynamic range of our workflow (Fig. 1C) [14] we were able to quantify an assortment of major ion channels and receptors known to be implicated in nociception and pain. This includes, for example, transient receptor potential vanilloid channel 1 (Trpv1), voltage-gated calcium channel subunits (e.g., Cacna2d1), voltage-gated sodium channels (e.g., Scn4b, Scn9a), and voltage-gated potassium channel subunits (e.g., Kcnab2, Kcna2) [35,36] (Fig. 1D, STable 1). Furthermore, our dataset captures the majority of previously reported myelin-associated proteins [7] (SFigure 2 F, STable 2). We also extended our recent data on the protein set-up of the sciatic nerve in naïve mice [14] (SFigure 2 G, STable 2) indicating the analysis depth and suitability of our workflow for profiling pathology-associated proteome dynamics in low input samples.

To determine nerve injury-induced proteome changes, we applied a significance cut-off (q-value $\leq$ 0.05) and determined differentially expressed proteins (DEPs; SNI versus Sham) at each time point after nerve injury. Respective volcano plots and overviews of all comparisons are shown in SFigure 3 (also listed in STable 3). Among these DEPs were several ion channels, which showed differential expression in dependence on sex, age, and time point (Fig. 1D, STable 3). It is noteworthy that the extent of proteome dynamics partly correlated with time after nerve injury (Fig. 1E-G). This hints at extensive proteome rearrangements (possibly for both de- and regenerative purposes, e.g., Wallerian degeneration [5]) following nerve injury, which may contribute to associated pathologies such as neuropathic pain. Nerve injury was accompanied by immense alterations in proteins associated with biological pathways implicated in immune signaling and inflammation in accordance with previous reports [37–40]. We quantified a prominent inflammatory signature consisting of several cytokines/chemokines and their receptors as well as immune/inflammatory signaling components across diverse immune cell types (e.g., T cells, B cells, neutrophils) (STable 4). Our results (Fig. 1E-G) also reveal similarities (sex-shared DEPs) and differences (sex-enriched DEPs) between sex and age groups at each time point, which strongly suggests that both sex and age shape the proteomic trajectory of the injured nerve (for an overview, please see sex-shared and sex-enriched DEPs in STable 5; age-dependent DEPs in STable 6). Bulk nerve proteomics cannot resolve cell type-specific protein changes. To indirectly infer cell type localization of DEPs, we leveraged the iSNAT atlas [28] transcriptome datasets at 7 days after injury (SFigure 4A-B; D7 vs. D0; D7 is the longest time point provided by iSNAT like our "early" time point D7; iSNAT data are mixed from male and female mice). Despite well-known differences in proteomics and transcriptomics [41]' [42] that limit the possible extent of overlap, we nevertheless detect biologically relevant trends in our proteome dataset: First, comparing our DEPs to iSNAT marker genes of cell types (SFigure 4 C; please see STable 7 for a full list of marker genes and overlapping proteins) support the notion that DEPs may be derived from diverse cell types of the sciatic nerve including (i) Schwann cells (SC), (ii) immune cells (e.g., macrophages, Mac; T cells, TC; natural killer cells, NK), and (iii) fibroblasts (Fb) just to name a few. Thus, our proteome data partly reflect iSNAT reported changes in some, but not all, cell type proportions after nerve injury (SFigure 4D) such as (i) the pronounced increase of SC (up to 25 % DEPs are also SC markers) and (ii) the increase of Mac. The observed representation of immune cells aligns with our finding of a prominent immune/inflammatory signature (STable 4). Second, comparing our bulk proteomics to differentially expressed genes (DEGs) within these cell types (SFigure 4E; please see STable 7 for a full list of transcript changes and overlapping proteins) suggested that changes detected in our proteome dataset partly reflect transcript changes in several cell types (e.g., SC, Fb, Mac, TC) albeit less so in mast cells [43] and NK cells (SFigure 4E). Of note, DEPs, which are sex-shared in our proteome dataset at early time points (D7 and D14 pooled) exhibit the highest match as expected from the iSNAT data structure (sex-mixed, up to D7).

Taken together, these results establish a comprehensive proteomic resource capturing the complexity of peripheral nerve responses to trauma and provide the foundation for future mechanism-based investigations.

3.2. MEFISTO reveals temporal latent patterns shaped by condition, sex, and developmental age

To disentangle the complex temporal dynamics of the sciatic nerve proteome following injury, we applied MEFISTO (MEssage FInding for Spatio-Temporal Ordering) [24], a latent factor model optimized for time-series multi-group omics data. MEFISTO has proven its utility for the system-level analysis of multimodal data such as mouse development [24], identification of COVID-19 severity markers [44], and in our recent study using the SNI model in mice [4].

MEFISTO identified several latent factors whose temporal trajectories captured variation across condition (SNI vs. Sham and Naïve), sex, and age (Fig. 2, SFigure 5, STable 8). Factor 22 and factor 31 effectively separated SNI from Sham and Naïve conditions reflecting how these factors encode variation associated with injury state, yet independent from sex and age (Fig. 2A). In contrast, factor 16, factor 24 and factor 36 were primarily associated with sex, as their trajectory values diverged between male and female mice across time points (Fig. 2B). Factor 34 separated samples by age, distinguishing 4-week-old from 12-week-old mice (Fig. 2C). Factor 46 also contributed to the separation, although its ability to distinguish age groups was only marginal.

To further dissect these patterns, we performed sex- and age-stratified MEFISTO analyses. In the sex-stratified model (SFigure 6 A), trajectory differences along factors 16, 24, and 36 revealed prominent condition- and sex-dependent shifts. In the age-stratified model (SFigure 6B), latent trajectories partly distinguished juvenile (4-week-old) from young adult (12-week-old) mice. Factor 34 was especially informative, separating samples by age pointing towards a trend to higher proteome dynamics over time in juvenile mice. These results demonstrate that we can capture latent temporal variation driven by sex, developmental stage, and nerve injury. Rather than indicating up- or downregulation of single proteins, the latent factors reflect structured, group-specific patterns within the proteome - emphasizing the value of dimensionality reduction for exploring the complexity of

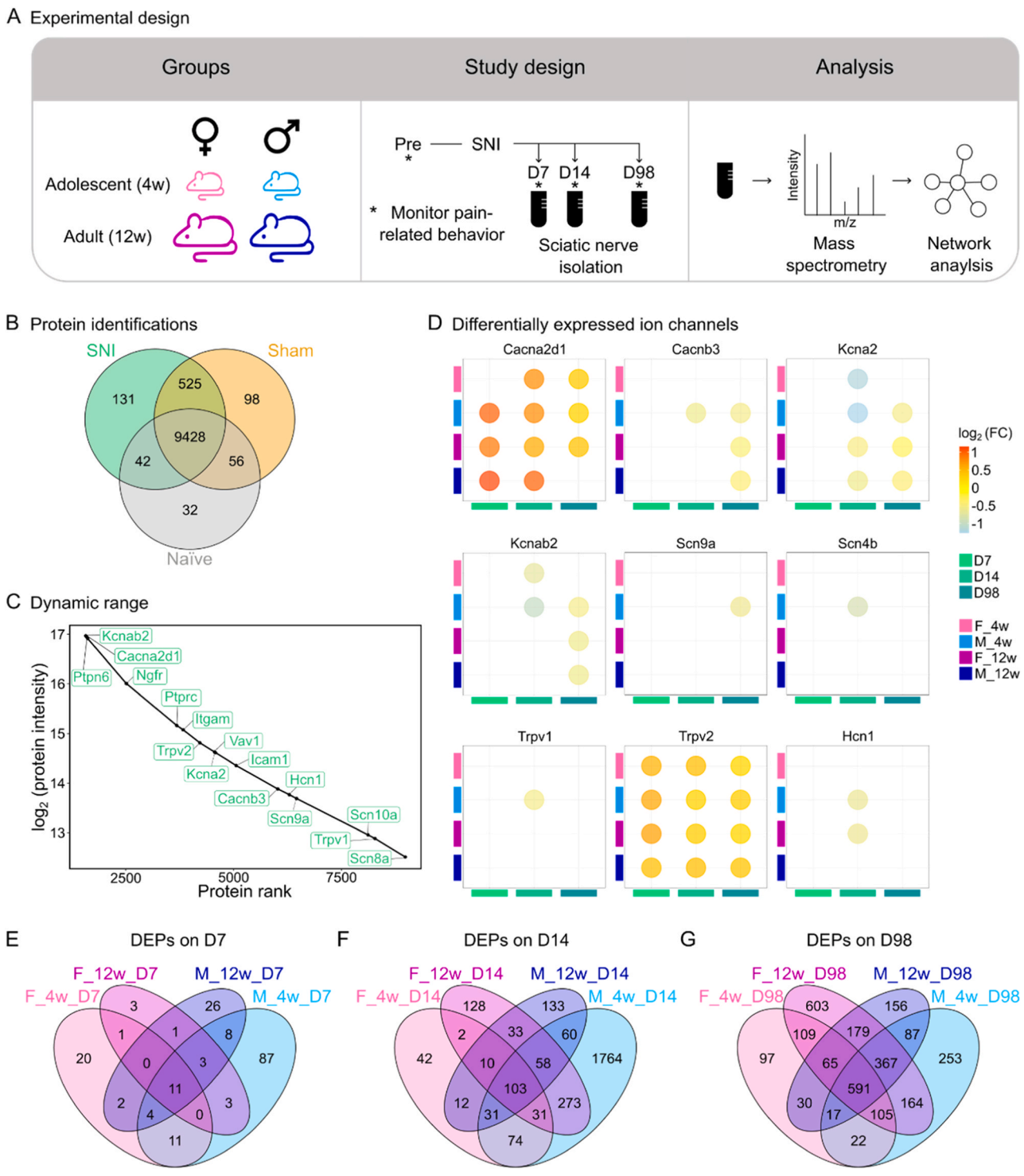

Fig. 1. Deep proteome profiling in mouse sciatic nerve upon nerve injury. (A) The experimental groups constituted of male and female mice of two age groups (adolescent – 4 weeks and adult – 12 weeks). We used the spared nerve injury (SNI) model to study nerve injury-induced proteome dynamics in the sciatic nerve. Control groups consisted of Sham-treated mice (skin incision without nerve injury) and, for proteomic analysis, naïve mice (no incision or nerve injury). Pain-related behaviors were investigated three to four days before nerve injury (Pre), early after nerve injury (D7 and D14), as well as late after injury (D98). At D7, D14 and D98 sciatic nerves were collected for proteomic analysis using LC-MS/MS with data-independent acquisition via parallel accumulation–serial fragmentation (DIA-PASEF). Proteomic data were subjected to network analysis to identify sex-, age-, and time point-dependent molecular signatures associated with nerve injury. (B) Venn diagram shows unique and shared protein groups (protein IDs) across experimental conditions (Naïve, Sham, SNI). In each condition more than 9000 protein groups were identified (see quantified protein groups in STable1). (C) Representative data of the dynamic range of protein abundance in SNI samples. The y-axis shows the log_2-transformed protein intensity. A selection of pain genes and ion channels known to be involved in nociception and pain are depicted to indicate their relative abundance. (D) Examples of differentially expressed ion channels when comparing SNI vs. Sham at indicated time points (D7, D14, and D98) and across sex and age groups. Color legend reflects log_2-transformed fold change (FC) derived from these SNI–Sham comparisons. (E-G) Venn diagrams show the number of DEPs between SNI vs. Sham (q-value ≤ 0.05) across sex and age groups on (E) D7, (F) D14 and (G) D98 (see STable 3 for DEPs per experimental group, STable 5 for sex-shared and sex-enriched DEPs, and STable 6 for age-shared and age-enriched DEPs).

biological responses to nerve injury.

3.3. Pathway associations of sex-linked latent factors reveal temporal and sex-biased regulation of the IFN-α response

Next, we integrated traditional differential expression analysis for sex-enriched DEPs (Fig. 1E-G, STable 5) with the results of MEFISTO-based latent factor modeling (Fig. 2, STable 8). Specifically, we matched sex-enriched DEPs identified at each post-injury time point (STable 9; for cut-off criteria please see methods) with proteins contributing to MEFISTO factors 16, 24 and 36, which indicated sex-associated variance over time but independent of age and nerve injury (STable 9). Despite using two very different analysis tools, we identified overlapping protein alterations (Fig. 3A-B; STable 9) and represented biological pathways (STable 8 for MEFISTO, STable 10 for sex-enriched DEP) highlighting the robustness of our data (Fig. 3C-D). Importantly, many sex-enriched DEPs matched transcriptome changes in peripheral nerves of human patients with neuropathy [45] (i.e. diabetic peripheral neuropathy, DPN) such as several eukaryotic translation initiation factors (*Eifs*), 10-formyltetrahydrofolate dehydrogenase (*Aldh1l1*), and FK506 binding protein 5 (*Fkbp5*) (please see full list of DEP-transcriptome overlaps in STable 11) highlighting the translational and cross-species significance of our mouse study.

Pathway enrichment (using GO-BP, gene ontology biological process) provided insights into the biological significance of sex-linked proteomic trajectories at early (combining DEPs from time points D7 and D14) and late (DEPs from D98) time points after nerve injury (Fig. 3C; details in STable 10). Besides many others (full list in STable 10), we observed pathways related to acute injury (response to stress, wounding, autophagy), molecular re-organization (vesicle-mediated transport, extracellular matrix), metabolism (e.g., of fatty acids), neuronal processes (neurogenesis, axon injury, synapse), glia and Schwann cell biology, and to immune-related and inflammatory processes (oxidative stress, innate immune response, cytokine response, T and B cell signaling).

While some of these pathways were identified in both female and male SCN (as expected given that pathways are composed of many proteins), our experimental design allowed us to discern sex and previously unknown temporal differences. For example, immune modulation appeared to be temporally divergent between sex – a finding with extends prior studies suggesting that neuropathic pain is accompanied by sexually dimorphic modulation of the immune system [4,33,46–48] showcasing the biological significance of our dataset. In contrast to females, male-enriched proteins were associated with immune-related pathways already at early time points (e.g., T cell proliferation, innate immune response, response to cytokines and interferon, IFN) lasting until the late phase. As IFN-related signaling has previously been implicated in neuropathic pain in mice and humans [3,49,50], we had a closer look at IFN-related pathways stratified by sex, age, and time. We did so using two approaches: comparison to IFN-associated genes by official GO-terminology (Fig. 3D) and by network biology (SFigure 7). In male mice, we observed an age-dependent biphasic regulation pattern: already at early time points the abundance of several interferon-associated proteins was altered with relatively more upregulation in 4w old males compared to 12 w old males (STable 6). These data suggest early and age-dependent immune modulation [51–54]. By D98, this profile shifted to a broad upregulation of IFN-related proteins, including canonical signaling hubs like *Stat1* and *Jak1*, consistent with engagement of the JAK/STAT pathway upon nerve injury. In contrast, female-enriched DEPs associated with IFN remained largely unchanged at early time points, but were mostly upregulated by D98 (Fig. 3D, SFigure 7).

Thus, although both sexes activate IFN signaling in response to peripheral nerve injury, the temporal pattern appears to be different. Males, in particular 4w old males, displayed initial and sustained modulation, while females engaged IFN signaling later.

3.4. Core temporal programs in sex-shared injury responses

In our previous work on sciatic nerves in naïve mice [14] and also on DRG proteome dynamics upon SNI [4], we highlighted the translational and clinical value of finding sex-shared molecular responses to nerve injury. Along these lines, here, we also analyzed sex-shared proteome alterations. Specifically, we matched sex-shared DEPs identified at each post-injury time point (STable 5; for cut-off criteria please see methods) with proteins contributing to MEFISTO factors 22 and 31, which represent injury-associated variance across time but independent of sex and age (STable 8). Similar to the sex-enriched analysis above (Fig. 3), we could show an overlap of many proteins (Fig. 4A, STable 12) and represented pathways (Fig. 4B, STable 13) using these two very different analysis tools. In accordance with the observed time-dependency of proteome alterations in general (Fig. 1), the number of sex-shared proteins increased with time after injury. This likely reflects the temporal dynamics of the injury response and highlights the importance for longitudinal studies [33] to investigate temporal patterns of injury-associated plasticity in the peripheral nerve.

Temporal biological pathway patterns were also evident for sex-shared proteins (Fig. 4B; for details of pathway analysis, included data, and complete results please see methods and STable 13). To better contrast early and late-phases, we categorized pathways across broader biological themes (Fig. 4B, STable 13). In both phases neuronal processes (*synaptic processes & neurotransmission; neural development*) and *lipid metabolism* as well as general *metabolic & homeostatic processes* were prominent. Late-phase changes prominently included *cell cycle control & DNA repair, gene expression & chromatin regulation* as well as broad cellular signaling (*cell signaling & hormone response, cellular response to ions)* besides altered metabolism. As metabolic changes are implicated in the pathology of nerve injury and pain [55,56] [57,58], we specifically looked at metabolism-related pathways among these sex-shared DEPs (Fig. 4C; STable 14). Early, diverse aspects of lipid-associated metabolism dominated including isoprenoids, which serve as source for steroid (e.g., cholesterol) synthesis. These processes were also present at the late phase, albeit with lower scores. In parallel, the late time point exhibited several processes related to carbohydrate metabolism (*glucose, fructose 6-phophate and small molecular biosynthesis*; please see STable 14 for distinct sex-shared DEPs associated to these processes). Not surprisingly given the predominance of metabolism-related pathways among sex-shared DEPs, both phases showed an overrepresentation of insulin signaling known to control metabolism, from glucose via proteins to lipids.

Taken together, we revealed insights into temporal reprogramming upon nerve injury: from acute neuronal regulation and metabolic rewiring to sustained metabolic changes, transcriptional tuning, and structural re-organization with possible implications for the development of chronic pain after nerve injury – an observation, which is supported by previous studies in the murine spinal cord [59] and in pain patients [3].

3.5. Network analysis suggests a sex-conserved transition from acute injury responses to large-scale remodelling

Finally, we visualized the temporal dynamics of sex-shared DEPs (from overlapping pathways with MEFISTO factors 22 and 31, STable 14) using comparative network analysis (Fig. 5). Early after nerve injury (Fig. 5A), we observed a sparse modular network with small clusters. These were primarily related to lipid metabolism (cyan, e.g., several *Apo proteins, Fdps, Lss, Hmgcs1*), neuron projection development (pink, e.g., *Gap43, Gfap, Dlg4, Stmn2*) and partly overlapped with vesicle-mediated transport (light green, e.g., *Pacsin1, Dnm1 and 3*).

By D98 (Fig. 5B), a substantial reorganization and extension of the proteomic network had occurred and the network appears dense with highly interconnected modules (for a full list and regulation direction please see STable 14). Two dominant modules of transcriptional

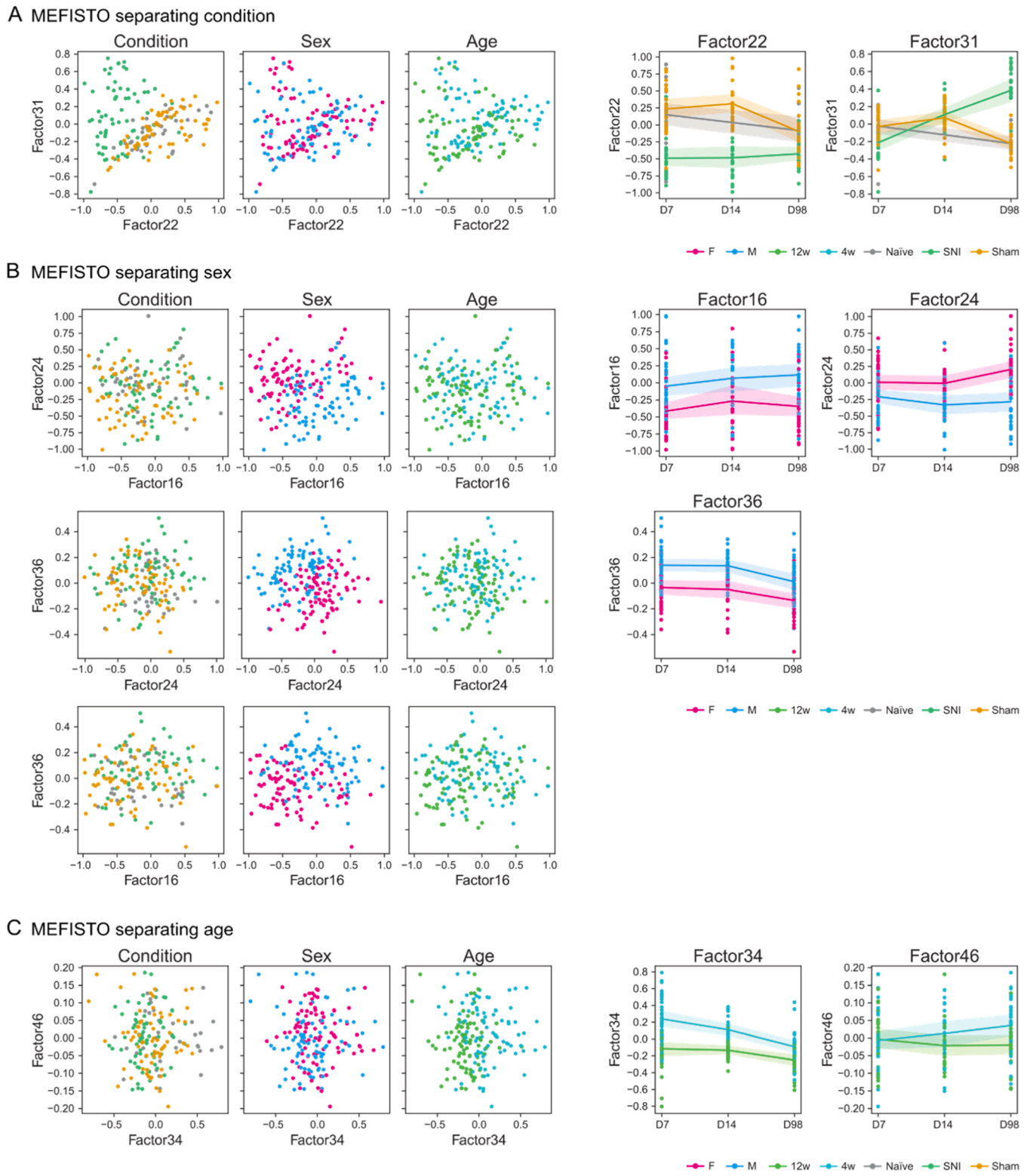

Fig. 2. Global MEFISTO-based factor analysis (A) MEFISTO factors 22 and 31 capture variances related to experimental condition (Naïve, Sham and SNI) (left). Plots on the right show factor values (factor 22 and 31) across time points for each sample. Solid lines indicate mean values for each group, transparent areas show the 95 % confidence interval around the group means. (B) Factor 16, 24 and 36 distinguish between sex (left). Plots on the right show factor values (factor 16, 24 and 36) across time points for each sample. Solid lines indicate mean values for each group, transparent areas show the 95 % confidence interval around the group means. (C) Factor 34 and 46 discriminate between age (left). Plots on the right show factor values (factor 34 and 46) across time points for each sample. Solid lines indicate mean values for each group, transparent areas show the 95 % confidence interval around the group means (see STable 8).

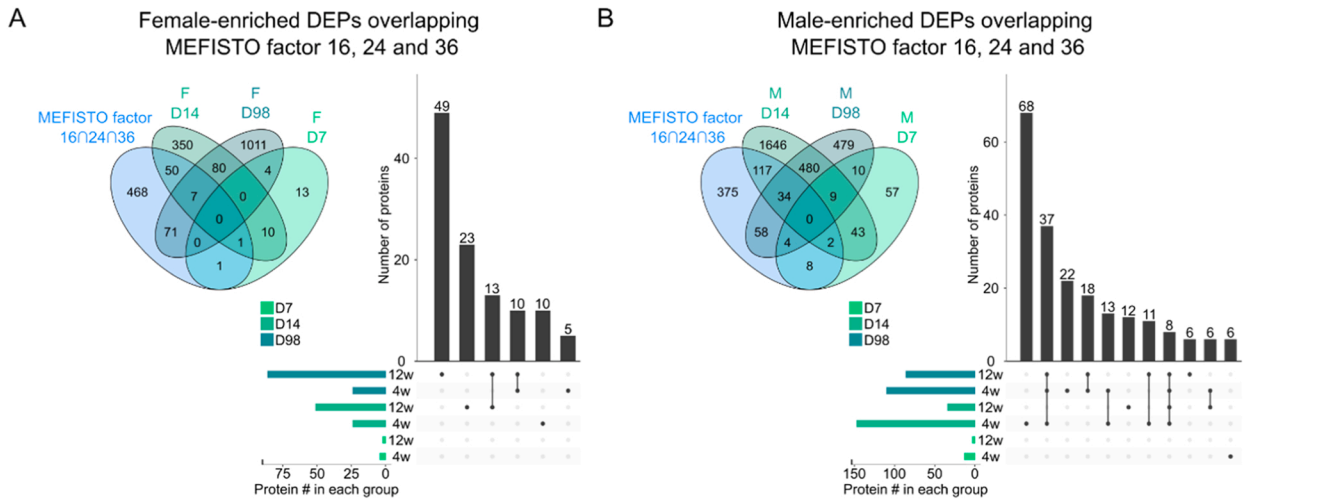

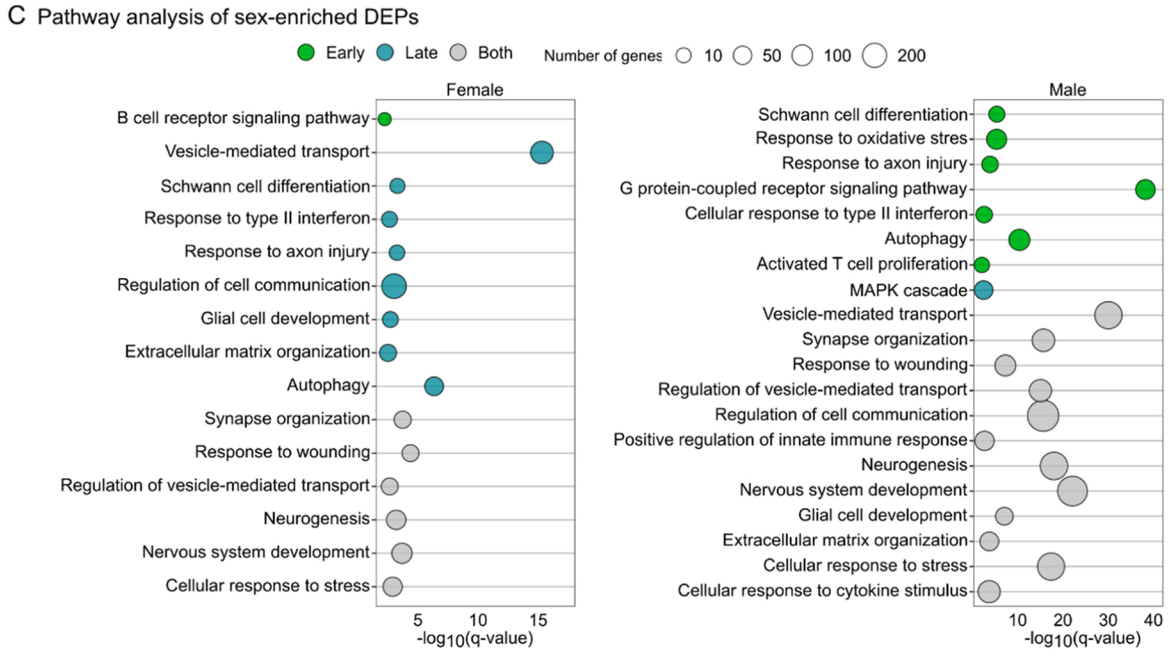

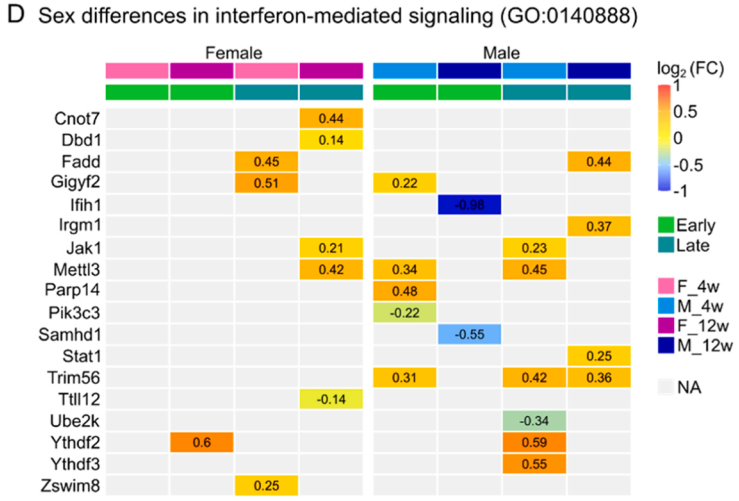

(caption on next page)

Fig. 3. Sex-enriched proteome dynamics and associated biological pathways. (A) Venn diagram compares proteins from MEFISTO factor 16, 24 and 36 and female-enriched DEPs across time points (D7, D14, D98). Upset plot shows the overlap of proteins from MEFISTO factor 16, 24 and 36 with female-enriched DEPs across age groups and time points (STable 9). (B) Venn diagram compares proteins from MEFISTO factor 16, 24 and 36 and male-enriched DEPs across time points (D7, D14, D98). Upset plot shows the overlap of proteins from MEFISTO factor 16, 24 and 36 with male-enriched DEPs across age groups and time points (STable 9). (C) A selection of biological processes (q-value $\leq$ 0.01, number of genes $>$ 5) from female-enriched DEPs (left) and male-enriched DEPs (right) are shown (full list in STable 10). Dot color indicates if a pathway was derived from early (light green; D7 & D14), late (dark green; D98) or both (grey) time points. If pathway derived from both time points, visualization is based on early time points. Dot size indicates the number of genes. X-axis shows the negative $\log_{10}$-transformed q-values. (D) Heatmap indicates relative expression (SNI vs. Sham) of DEPs associated with the interferon-mediated signaling pathway (GO:0140888). Color legend reflects $\log_2$-transformed fold change (FC) derived from SNI-Sham comparisons. NA (grey) indicates proteins not found as differentially regulated (DEP; SNI-Sham comparisons).

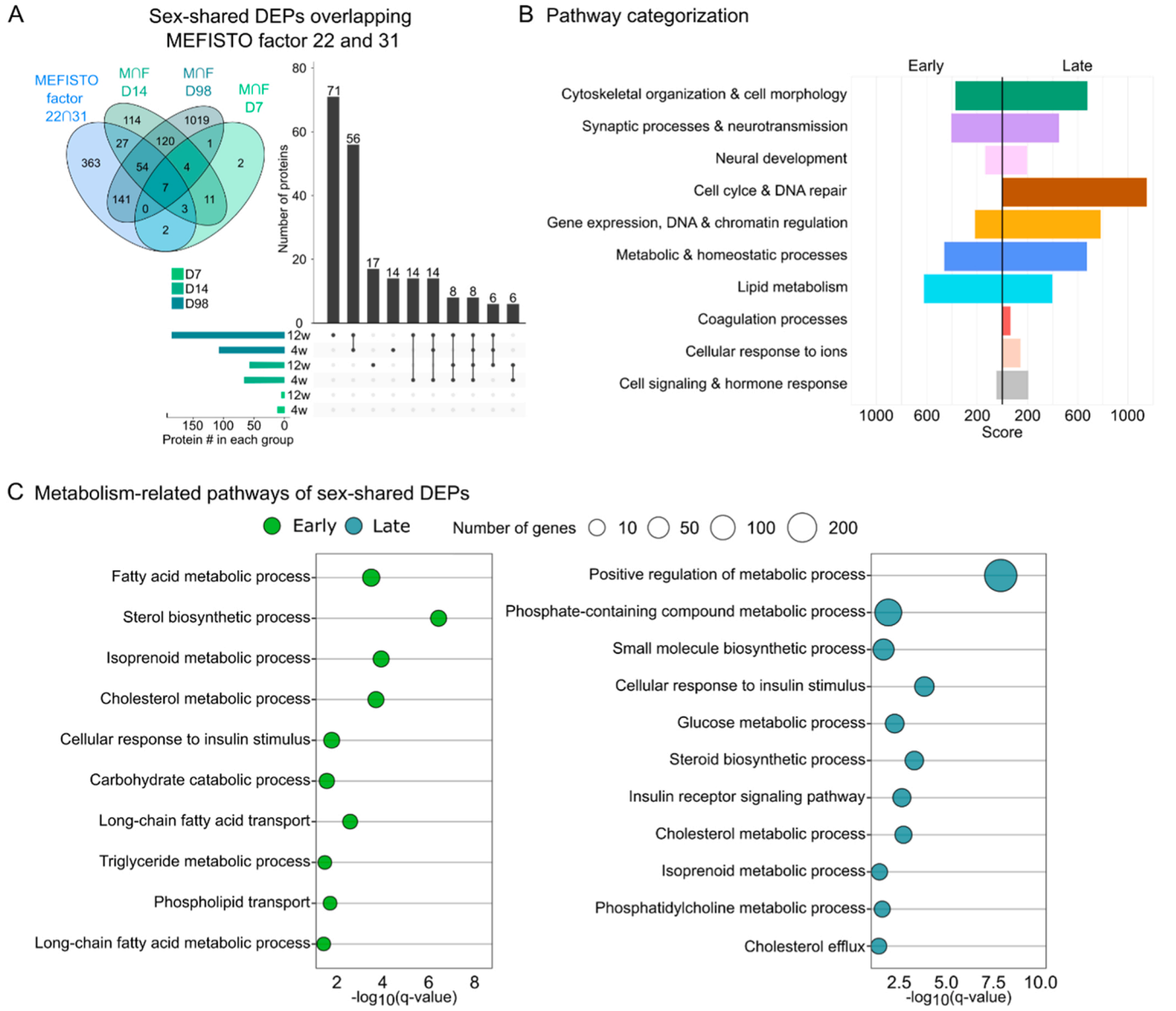

Fig. 4. Sex-shared proteome dynamics and associated biological pathways. (A) Venn diagram compares proteins from MEFISTO factor 22 and 31 and sex-shared DEPs across time points (D7, D14, D98). Upset plot shows the overlap of proteins from MEFISTO factor 22 and 31 with sex-shared DEPs across age groups and time points (STable 12). (B) Categorization of pathways overlapping (based on GO ID) between MEFISTO factor 22 and 31 pathway analysis (p-value $\leq$ 0.05; STable 8) and sex-shared DEP pathway analysis (q-value $\leq$ 0.05; STable 13). Score indicates the summarized (within each category) combined score (STable 13). Left, early after SNI (D14; no pathway result for D7); right, late after SNI (D98). (C) A selection of pathways from the categories metabolic & homeostatic processes, lipid metabolism and cell signaling & hormone response from (B) are shown. Visualization was based on sex-shared DEPs (STable 14). Dot size indicates the number of genes. X-axis shows the negative $\log_{10}$-transformed q-values. Left, early after SNI (D14; no pathway result for D7); right, late after SNI (D98). Dot color indicates early/late.

(yellow) and chromatin regulators (orange; e.g., SMARC chromatin remodelers such as *Smarca2, Smarca4;* histone variants such as *H2az1, H2bc12, H3f3b alias H3–3a, Hdac 1 and 2*) were upregulated, alongside multiple proteins implicated in cell cycle control (dark brown, e.g., Rac,1, Cdk4, Cdkn2), DNA repair (light brown, e.g., high mobility group proteins such *Hmgb1–3, several Hdgf* proteins), and ribonucleoprotein family members (orange-red; e.g., *hnRNPs*). Another prominent group were proteins implicated in cytoskeleton organization (dark green, e.g., *Arpc* family members, *Ptpn1*, Laminin family members, *Lmns*) and vesicle-mediated transport (light green, e.g., *Pacsins*, Nsf, Dynamin family members, *Dnms*), as well as neuronal function such as synapse organization (purple, e.g., Cacnb3, Nefh) and neuronal projections (pink, e.g., Dlg4, Arhgap35, Plp1). Additionally, proteins associated with lipid metabolism formed 2 smaller subnetworks (cyan, e.g., *Apo* family members, *Lss, Fdps*). Again, we could validate the translational and cross-species relevance of 203 DEPs (of which 31 and 73 are sex-shared in the early and late phase, respectively, full list in STable 15), which match transcriptome changes in nerves from DPN patients [45] (203/380 DEP-hNerve overlaps show concordant regulation; examples are highlighted with a red circle in Fig. 5; full list in STable 15).

4. Discussion

Our comprehensive proteomic analysis of sciatic nerve responses in a mouse model of spared nerve injury (SNI) provides novel insights into the molecular mechanisms triggered by nerve injury, revealing key aspects shaped by sex, developmental stage, and temporal dynamics.

In particular the latter, i.e., temporal dynamics, addresses a major challenge in the field. Most published molecular studies on peripheral nerve injury focus on early to mid-range phases (0–28 days), while the molecular landscape at chronic time points beyond 8 weeks remains strikingly underexplored in murine pain models. This is especially important given that long-term behavioral sequelae and persistent neuropathic pain are well documented in animal models and their understanding is crucial for translationally relevant research [33] [60] [61] [62].

Notably, our work focuses on the axonal compartment of the peripheral nerve. In contrast to very extensively studied somata of DRG, axon responses have been studied far less in the context of neuropathic pain. The sciatic nerve is (i) a major conduit for both sensory input and motor output, (ii) crucially implicated in de- and regeneration in the context of peripheral pathologies, (iii) implicated in nerve injury-triggered neuropathic pain, and (iv) more accessible for therapeutic targeting than DRG somata. Consequently, our work fills a critical gap in preclinical research and provides a framework for further mechanistic studies and peripheral therapeutic targeting.

The use of MEFISTO [24], a latent factor model for time-series -omics data, enabled us to deeply explore the temporal complexity in dependence on sex and developmental age. We identified proteins and associated pathways that exhibit sexual dimorphism, many of which were also altered in nerves of patients with neuropathy [45] (STable 11), validating the biological significance of our findings. Sex-stratified temporal differences were prominent in the immune/inflammatory signature (Fig. 3C), such as in the case of IFN-related signaling (Fig. 3D). Males engaged IFN-related signaling early after injury (in particular 4w old young males) followed by activation of canonical Stat1-Jak1 signaling at D98. This pattern is in accordance with reported associations between chronic inflammation, sustained IFN signaling, and persistent neuropathic pain, but also anti-nociceptive actions of IFN responses have been reported [49,63–65]. For example, neuronal STING, a central regulator of innate immune responses and antiviral IFN-I signaling, is critically involved in nociception [49] in male and female mice. Both, its inhibition [64] and activation [49,65] has, depending on context, shown promising anti-nociceptive immunomodulation to provide pain relief early (at D12-D28) after nerve injury. In our study females presented with late activation of different interferon-stimulated candidates possibly indicative of sexually dimorphic immune strategies downstream of IFN [3,38,52]. While the mechanisms and sexual dimorphism of IFN-stimulated signaling across published studies require further clarification, its translational relevance to neuropathic pain is increasingly recognized. In female neuropathic pain patients undergoing thoracic vertebrectomy, Ray and colleagues [3] identified a female-specific correlation of distinct IFN-associated gene signatures and pain [3].

Here, we complement and extend the knowledge on the molecular landscape after nerve injury by providing a longitudinal view on early and late time points. Our data may be harnessed for time- and sex-aware preclinical and translational research and drug target testing. For example, FDA-approved Jak inhibitors (Ruxolitinib and Baricitinib – indicated for myeloproliferative and autoimmune disorders) could potentially modulate IFN-driven processes, though sex- and time-specific efficacy would need careful evaluation.

In addition, we revealed sex-shared temporal proteomic signatures, which may delineate a core response to nerve injury. Early post-injury phases were enriched for neuronal remodeling and metabolic adjustments, aligning with acute injury and repair processes [12,66]. Indeed, metabolic reprogramming and lipid metabolism are intricately linked to the development and persistence of chronic pain. For example, the cysteine amidase NAAA (one of our DEPs, which were downregulated at early time points but upregulated at late time points, STable 3) is suggested to be a potential driver of chronic pain upon nerve injury. NAAA hydrolyzes palmitoylethanolamide (PEA), a lipid mediator produced by sensory neurons and macrophages that sustains PPAR-α–mediated anti-inflammatory and antinociceptive signaling [55,56]. Following tissue injury, increased NAAA activity lowers PEA availability, dampening PPAR-α activation and thereby amplifying inflammatory responses [57]. Consistent with this mechanism, pharmacological NAAA inhibitors restore PEA signaling, suppress neuroinflammation, and alleviate pain behaviors in rodent models of nerve injury and peripheral inflammation even upon topical application [57,58]. Together, these findings suggest that differential dynamics of NAAA and, potentially, other metabolic regulators observed in our proteomic dataset (e.g., Fig. 4B-C and STables 13 and 14) are part of broader metabolic reprogramming early and late after nerve injury that may ultimately contribute to neuropathic pain. Remarkably, recent investigations leveraged this knowledge for successful relief of postsurgical pain via modified nutrition [55].

Late after injury (D98), metabolic changes were sustained alongside pronounced transcriptional and structural reorganization in accordance with findings in neuropathic pain patients [3,45] and likely contributed by non-neuronal proliferating cell types [3] (please see iSNAT analysis across cell types in SFigure 4, STable 7). Network analyses reinforced this concept. For example, key regulators such as histone deacetylase HDAC2, SMARC (SWI/SNF-related matrix-associated actin-dependent regulator of chromatin) proteins, and HMGB1 (High--Mobility-Group-Protein) emerged as highly connected nodes (Fig. 5). These proteins may serve as mechanistic anchors for future translational studies and potential drug repurposing. HDAC inhibitors such as Vorinostat and Romidepsin - both FDA-approved for the treatment of cutaneous T-cell lymphoma - are compelling candidates. Preclinical studies have demonstrated that intrathecal or systemic HDAC inhibition reduces mechanical hypersensitivity in neuropathic pain models [67–69]. Additionally, HMGB1 antagonists such as glycyrrhizin - a natural anti-inflammatory and neuroprotective compound used in traditional medicine - have been shown to inhibit HMGB1 release [70], thereby reducing inflammatory and neuropathic pain behaviors [71, 72]. Thus, both HDAC inhibitors and HMGB1 antagonists merit further investigation as potential disease-modifying agents for chronic nerve injury and neuropathic pain. Proteins of the sex-shared core proteome signatures identified here were also altered in nerves from neuropathy patients [45] (STable 15) and, thus, provide strong translational value: by focusing on what is conserved rather than divergent across biological

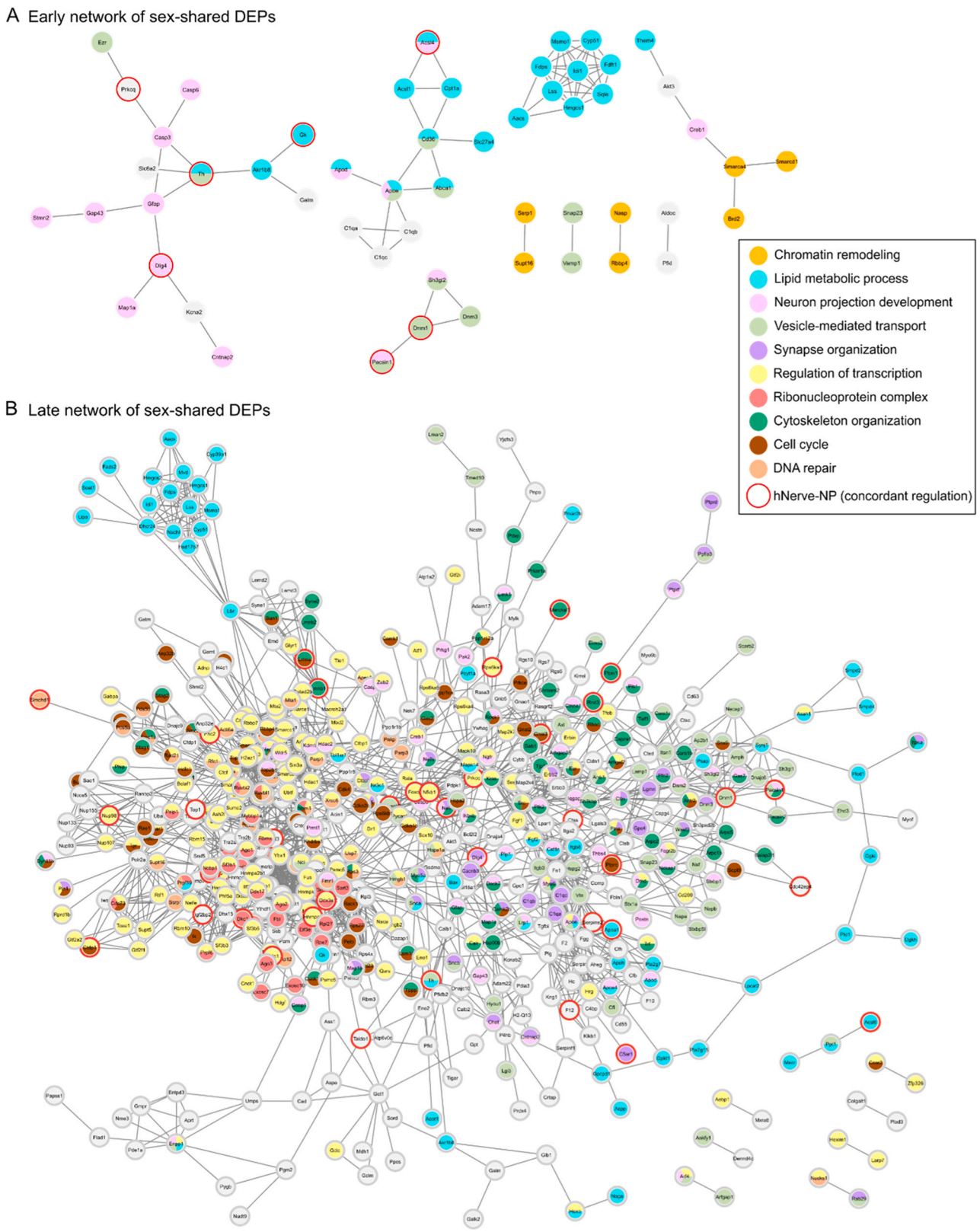

Fig. 5. Protein interaction networks of sex-shared DEPs across early and late phases after SNI. (A-B) Protein-protein interaction network of sex-shared DEPs (derived from Fig. 4B-C, STable 14) retrieved from STRING (v12.0) [27] and Cytoscape (v3.10.1) [25]. This interaction map was generated using high confidence (0.7). Node color reflects pathway association. Nodes with a red border show concordant regulation in nerves from neuropathic pain patients [45] (hNerve-NP = human nerve neuropathic pain). Nodes without any connection are hidden from the networks. (A) Network of sex-shared DEPs early (D7-D14) after SNI. (B) Network of sex-shared DEPs late (D98) after SNI.

subgroups, these signatures open avenues for therapeutic discovery that may be broadly applicable across diverse populations, including adolescents, adult men, and women.

At the same time, several limitations of our study should be acknowledged. While we captured early and late stages of the injury response, even longer observation times extending to several months after nerve injury will be necessary to fully delineate the chronic trajectory [33,43,59]. Moreover, our study did not include senior mice. Given that biological aging and sex interact in complex ways to shape systemic metabolism and recovery after nerve injury [33,43,48,73,74], integrating aged cohorts will be essential to understand how metabolic resilience or vulnerability influences pain outcomes across the lifespan.

Another limitation is that our approach relied on bulk proteomics of the sciatic nerve – a heterogeneous tissue comprising axons, Schwann cells, fibroblasts, endothelial cells, resident macrophages, and infiltrating immune cells. Thus, we could only infer protein changes to cell types using transcriptome data of iSNAT (SFigure 4). While single-cell methods provide cell-type resolution, they are not well suited to capture distal axons, consequently iSNAT does not contain data about the actual axon. As a promising alternative, cell type–specific proximity labeling strategies (e.g., TurboID-based proteomics) have recently emerged [75] and allow tagging of proteins from defined cell populations within intact tissue environments. We have recently applied such approaches in peripheral nerve, enabling profiling of axons and terminals [76], which can be integrated with datasets to dissect cell-autonomous versus non-autonomous responses. Finally, although translation to human pathology remains a challenge, many dozens of here identified DEPs match transcript alterations in human neuropathic nerves [45], providing cross-species validation.

Future work integrating this proteome resource with spatial, single-cell, and functional analyses in both preclinical and translational models will be critical to establish causal mechanisms and guide targeted interventions for neuropathic pain.

5. Conclusion

In summary, our longitudinal, demographically inclusive proteomic analysis of the injured sciatic nerve provides a temporal framework of nerve injury-induced alterations. We captured sex- and age-divergent molecular trajectories alongside conserved sex-shared patterns. Therefore, our study offers a comprehensive view of the dynamic molecular landscape upon nerve injury fostering future cross-species, cell type–resolved, and translational investigations.

Data availability

Requests for materials should be directed to and will be fulfilled by the Lead Contact, Manuela Schmidt (manuela_schmidt@univie.ac.at). The mass spectrometry proteomics data have been deposited to the ProteomeXchange Consortium via the PRIDE [77] partner repository with the dataset identifier PXD067006. MEFISTO analysis code has been deposited at Zenodo and will be publicly available as of the date of publication. DOI: https://doi.org/10.5281/zenodo.16737895 (https://github.com/menchelab/Grundtner_et_al_2025). Any additional information required to reanalyze the data reported in this paper is available from the lead contact upon request. All code for the iSNAT analysis can be found here: https://github.com/aliibarry/mSN_proteomics

CRediT authorship contribution statement

Jörg Menche: Supervision, Resources. **Allison Marie Barry:** Formal analysis, Visualization, Writing – review & editing. **Julia Regina Sondermann:** Writing – review & editing, Validation, Supervision, Investigation, Conceptualization. **Tina Radits:** Investigation, Formal analysis, Data curation. **Daniel Malzl:** Writing – review & editing, Visualization, Investigation, Formal analysis, Data curation. **Manuela Schmidt:** Writing – review & editing, Writing – original draft, Supervision, Project administration, Funding acquisition, Formal analysis, Data curation, Conceptualization. **Gomez-Varela David:** Supervision, Resources, Conceptualization. **Sabrina Grundtner:** Writing – review & editing, Writing – original draft, Visualization, Validation, Methodology, Formal analysis, Data curation, Conceptualization. **Feng Xian:** Writing – review & editing, Visualization, Validation, Investigation, Formal analysis, Data curation.

Funding

This research was funded in part by the Austrian Science Fund (FWF) [10.55776/P36554 and 10.55776/P35856, both to MS] and the University of Vienna.

Declaration of Competing Interest

The authors declare that they have no known competing financial interests or personal relationships that could have appeared to influence the work reported in this paper: MS received research awards and travel support by the German Pain Society (DGSS) both of which were sponsored by Astellas Pharma GmbH (Germany). MS received research awards by the Austrian Pain Society. MS received one-time consulting honoraria by Grunenthal GmbH (Germany). None of these sources influenced the content of this study, and MS declares no conflict of interest. DGV and MS have an ongoing scientific collaboration with Bruker (Bruker Center of Excellence for Metaproteomics, University of Vienna), however, this collaboration did not influence the content of the manuscript.

All authors declare that they have no conflicts of interest.

Acknowledgments

The authors would like to thank Nicole Kanta for excellent technical assistance, and Verena Hofer and Lea Weiss for help with tissue isolation (all: Systems Biology of Pain laboratory; Division of Pharmacology and Toxicology). We are grateful to Herbert Gasser (Faculty of Life Sciences, University of Vienna) for support with animal welfare, Dr. Daniel Segelcke (University Hospital Münster, Germany) for valuable advice on behavioral analysis, and our team of administrative personnel and animal caretakers for their outstanding support. Parts of the computational results of this work have been achieved using the Life Science Compute Cluster (LiSC) of the University of Vienna.

Appendix A. Supporting information

Supplementary data associated with this article can be found in the online version at doi:10.1016/j.biopha.2025.118855.

References

[1] R.Y. North, et al., Electrophysiological and transcriptomic correlates of neuropathic pain in human dorsal root ganglion neurons, Brain 142 (2019) 1215–1226.
[2] P. Ray, et al., Comparative transcriptome profiling of the human and mouse dorsal root ganglia: an RNA-seq-based resource for pain and sensory neuroscience research, Pain 159 (2018) 1325–1345.
[3] P.R. Ray, et al., RNA profiling of human dorsal root ganglia reveals sex-differences in mechanisms promoting neuropathic pain, Brain (2022).
[4] S. Grundtner, et al., Deep proteomics and network pharmacology reveal sex- and age-shared neuropathic pain signatures in mouse dorsal root ganglia, Pharm. Res. 211 (2025) 107552.
[5] L. Conforti, J. Gilley, M.P. Coleman, Wallerian degeneration: an emerging axon death pathway linking injury and disease, Nat. Rev. Neurosci. 15 (2014) 394–409.
[6] D. Romeo-Guitart, C. Casas, Network-centric medicine for peripheral nerve injury: treating the whole to boost endogenous mechanisms of neuroprotection and regeneration, Neural Regen. Res. 14 (2019) 1122–1128.
[7] S.B. Siems, et al., Proteome profile of peripheral myelin in healthy mice and in a neuropathy model, Elife 9 (2020).

[8] W. Zhang, et al., SARM1 activation promotes axonal degeneration via a two-step phase transition, Nat. Chem. Biol. (2025).
[9] I. Decosterd, C.J. Woolf, Spared nerve injury: an animal model of persistent peripheral neuropathic pain, Pain 87 (2000) 149–158.
[10] Flurkey, K., Currer, J.M. & Harrison, D.E., Vol. III 637-672 (Elsevier, 2007).
[11] O. Florez-Vargas, et al., Bias in the reporting of sex and age in biomedical research on mouse models, Elife 5 (2016).
[12] E.J. Cobos, et al., Mechanistic differences in neuropathic pain modalities revealed by correlating behavior with global expression profiling, Cell Rep. 22 (2018) 1301–1312.
[13] A.M. Barry, N. Zhao, X. Yang, D.L. Bennett, G. Baskozos, Deep RNA-seq of male and female murine sensory neuron subtypes after nerve injury, Pain 164 (2023) 2196–2215.
[14] F. Xian, J.R. Sondermann, D. Gomez Varela, M. Schmidt, Deep proteome profiling reveals signatures of age and sex differences in paw skin and sciatic nerve of naïve mice, Elife 11 (2022).
[15] R.E. Sorge, et al., Olfactory exposure to males, including men, causes stress and related analgesia in rodents, Nat. Methods 11 (2014) 629–632.
[16] M. Zimmermann, Ethical guidelines for investigations of experimental pain in conscious animals, Pain 16 (1983) 109–110.
[17] I. Decosterd, C.J. Woolf, Spared nerve injury: an animal model of persistent peripheral neuropathic pain, Pain 87 (2000) 149–158.
[18] D. Gómez-Varela, et al., Increasing taxonomic and functional characterization of host-microbiome interactions by DIA-PASEF metaproteomics, Front. Microbiol. 14 (2023) 1258703.
[19] E.M. Pogatzki-Zahn, et al., A proteome signature for acute incisional pain in dorsal root ganglia of mice, Pain 162 (2021) 2070–2086.
[20] J. Schindelin, et al., Fiji: an open-source platform for biological-image analysis, Nat. Methods 9 (2012) 676–682.
[21] C.S. Hughes, et al., Single-pot, solid-phase-enhanced sample preparation for proteomics experiments, Nat. Protoc. 14 (2019) 68–85.
[22] Team, R.C., Edn. 2023.12.1+402 (R Foundation for Statistical Computing, Vienna, Austria.; 2021).
[23] R. Argelaguet, et al., MOFA+: a statistical framework for comprehensive integration of multi-modal single-cell data, Genome Biol. 21 (2020) 111.
[24] B. Velten, et al., Identifying temporal and spatial patterns of variation from multimodal data using MEFISTO, Nat. Methods 19 (2022) 179–186.
[25] P. Shannon, et al., Cytoscape: a software environment for integrated models of biomolecular interaction networks, Genome Res. 13 (2003) 2498–2504.
[26] G. Bindea, et al., ClueGO: a Cytoscape plug-in to decipher functionally grouped gene ontology and pathway annotation networks, Bioinformatics 25 (2009) 1091–1093.
[27] N.T. Doncheva, J.H. Morris, J. Gorodkin, L.J. Jensen, Cytoscape StringApp: network analysis and visualization of proteomics data, J. Proteome Res. 18 (2019) 623–632.
[28] X.F. Zhao, et al., The injured sciatic nerve atlas (iSNAT), insights into the cellular and molecular basis of neural tissue degeneration and regeneration, Elife 11 (2022).
[29] B. Parks, W. Greenleaf, Scalable high-performance single cell data analysis with BPCells, bioRxiv (2025).
[30] Y. Hao, et al., Dictionary learning for integrative, multimodal and scalable single-cell analysis, Nat. Biotechnol. 42 (2024) 293–304.
[31] D. Segelcke, B. Pradier, S. Reichl, L.C. Schäfer, E.M. Pogatzki-Zahn, Investigating the role of Ly6G(+) neutrophils in incisional and inflammatory pain by multidimensional, Pain. Relat. Behav. Assess. Bridg. Transl. Gap. Front Pain. Res (Lausanne) 2 (2021) 735838.
[32] D. Segelcke, et al., Tmem160 contributes to the establishment of discrete nerve injury-induced pain behaviors in male mice, Cell Rep. 37 (2021) 110152.
[33] M. Millecamps, S.G. Sotocinal, J.S. Austin, L.S. Stone, J.S. Mogil, Sex-specific effects of neuropathic pain on long-term pain behavior and mortality in mice, Pain (2022).
[34] F. Meier, et al., diaPASEF: parallel accumulation-serial fragmentation combined with data-independent acquisition, Nat. Methods 17 (2020) 1229–1236.
[35] F. De Logu, P. Geppetti, Ion channel pharmacology for pain modulation, Handb. Exp. Pharm. 260 (2019) 161–186.
[36] M. Ślęczkowska, K. Misra, S. Santoro, M.M. Gerrits, J.G.J. Hoeijmakers, Ion channel genes in painful neuropathies, Biomedicines 11 (2023).
[37] A.J. Davies, et al., Natural Killer Cells Degenerate Intact Sensory Afferents following Nerve Injury, Cell 176 (2019) 716–728.
[38] R.E. Sorge, et al., Different immune cells mediate mechanical pain hypersensitivity in male and female mice, Nat. Neurosci. 18 (2015) 1081–1083.
[39] M. Davoli-Ferreira, et al., Regulatory T cells counteract neuropathic pain through inhibition of the Th1 response at the site of peripheral nerve injury, Pain 161 (2020) 1730–1743.
[40] J.R. Bethea, R. Fischer, Role of peripheral immune cells for development and recovery of chronic pain, Front. Immunol. 12 (2021).
[41] E.G. Williams, et al., Systems proteomics of liver mitochondria function, Science 352 (2016) aad0189.
[42] J. Wang, et al., Proteome profiling outperforms transcriptome profiling for coexpression based gene function prediction, Mol. Cell. Proteom. MCP 16 (2017) 121–134.
[43] S. Marinelli, et al., Metabolic resilience rules sex-specific pain recovery during hormonal aging: a multi-omics analysis of neuropathy in mice, bioRxiv (2025).
[44] J.S. Gisby, et al., Multi-omics identify falling LRRC15 as a COVID-19 severity marker and persistent pro-thrombotic signals in convalescence, Nat. Commun. 13 (2022) 7775.
[45] D. Tavares-Ferreira, et al., Cell and molecular profiles in peripheral nerves shift toward inflammatory phenotypes in diabetic peripheral neuropathy, J. Clin. Invest 135 (2025).
[46] J.S. Mogil, Sex differences in pain and pain inhibition: multiple explanations of a controversial phenomenon, Nat. Rev. Neurosci. 13 (2012) 859–866.
[47] J.C. Mapplebeck, S. Beggs, M.W. Salter, Sex differences in pain: a tale of two immune cells, Pain 157 (1) (2016).
[48] N.L. Dos Santos, et al., Age and sex drive differential behavioral and neuroimmune phenotypes during postoperative pain, Neurobiol. Aging (2022).
[49] C.R. Donnelly, et al., STING controls nociception via type I interferon signalling in sensory neurons, Nature 591 (2021) 275–280.
[50] U. Franco-Enzastiga, et al., Type I IFNs enhance human dorsal root ganglion nociceptor excitability and induce TRPV1 sensitization, JCI Insight 10 (2025).
[51] A.M. Gregus, I.S. Levine, K.A. Eddinger, T.L. Yaksh, M.W. Buczynski, Sex differences in neuroimmune and glial mechanisms of pain, Pain 162 (2021) 2186–2200.
[52] J.C.S. Mapplebeck, S. Beggs, M.W. Salter, Sex differences in pain: a tale of two immune cells, Pain 157 (1) (2016) S2–s6.
[53] J.X. Yang, et al., Potential neuroimmune interaction in chronic pain: a review on immune cells in peripheral and central sensitization, Front Pain. Res (Lausanne) 3 (2022) 946846.
[54] E. Meade, M. Garvey, The role of neuro-immune interaction in chronic pain conditions; functional somatic syndrome, neurogenic inflammation, and peripheral neuropathy, Int J. Mol. Sci. 23 (2022).
[55] A.M. Tagne, et al., Metabolic reprogramming in the spinal cord drives the transition to pain chronicity, bioRxiv (2025).
[56] Y. Fotio, et al., NAAA-regulated lipid signaling governs the transition from acute to chronic pain, Sci. Adv. 7 (2021) eabi8834.
[57] C. Solorzano, et al., Selective N-acylethanolamine-hydrolyzing acid amidase inhibition reveals a key role for endogenous palmitoylethanolamide in inflammation, Proc. Natl. Acad. Sci. USA 106 (2009) 20966–20971.
[58] O. Sasso, et al., Antinociceptive effects of the N-acylethanolamine acid amidase inhibitor ARN077 in rodent pain models, Pain 154 (2013) 350–360.
[59] K.C. Lister, et al., Translational control in the spinal cord regulates gene expression and pain hypersensitivity in the chronic phase of neuropathic pain, bioRxiv (2024).
[60] Wood, J., N. & Mogil, J., S.. (Oxford University Press, 2019).
[61] K.E. Sadler, J.S. Mogil, C.L. Stucky, Innovations and advances in modelling and measuring pain in animals, Nat. Rev. Neurosci. 23 (2022) 70–85.
[62] T.J. Price, et al., Transition to chronic pain: opportunities for novel therapeutics, Nat. Rev. Neurosci. (2018).
[63] W. Liedtke, STING-ing pain: how can pro-inflammatory signaling attenuate pain? Neurosci. Bull. 37 (2021) 1075–1078.
[64] W. Wu, et al., Pharmacological inhibition of the cGAS-STING signaling pathway suppresses microglial M1-polarization in the spinal cord and attenuates neuropathic pain, Neuropharmacology 217 (2022) 109206.
[65] M. Defaye, et al., Induction of antiviral interferon-stimulated genes by neuronal STING promotes the resolution of pain in mice, J. Clin. Investig. 134 (2024).
[66] M. Costigan, J. Scholz, C.J. Woolf, Neuropathic pain: a maladaptive response of the nervous system to damage, Annu. Rev. Neurosci. 32 (2009) 1–32.
[67] M.V. Centeno, M.S. Alam, K. Haldar, A. Vania Apkarian, A Triple combination formulation of an HDAC inhibitor treats chronic pain in rodent spared nerve injury model, J. Pain. 31 (2025) 105396.
[68] M.N. Romanelli, V. Borgonetti, N. Galeotti, Dual BET/HDAC inhibition to relieve neuropathic pain: recent advances, perspectives, and future opportunities, Pharm. Res 173 (2021) 105901.
[69] F. Denk, et al., HDAC inhibitors attenuate the development of hypersensitivity in models of neuropathic pain, Pain 154 (2013) 1668–1679.
[70] P. Feldman, M.R. Due, M.S. Ripsch, R. Khanna, F.A. White, The persistent release of HMGB1 contributes to tactile hyperalgesia in a rodent model of neuropathic pain, J. Neuroinflamm. 9 (2012) 180.
[71] V. Thakur, J. Sadanandan, M. Chattopadhyay, High-mobility group box 1 protein signaling in painful diabetic neuropathy, Int. J. Mol. Sci. 21 (2020).
[72] P. Presto, G. Ji, O. Ponomareva, I. Ponomarev, V. Neugebauer, Hmgb1 silencing in the amygdala inhibits pain-related behaviors in a rat model of neuropathic pain, Int. J. Mol. Sci. 24 (2023).
[73] M. Millecamps, et al., The geriatric pain experience in mice: intact cutaneous thresholds but altered responses to tonic and chronic pain, Neurobiol. Aging 89 (2020) 1–11.
[74] V. Vacca, et al., Sex-specific adipose tissue's dynamic role in metabolic and inflammatory response following peripheral nerve injury, iScience 26 (2023) 107914.
[75] K.F. Cho, et al., Proximity labeling in mammalian cells with TurboID and split-TurboID, Nat. Protoc. 15 (2020) 3971–3999.
[76] J.R. Sondermann, et al., Proximity labelling reveals the compartmental proteome of murine sensory neurons, bioRxiv (2025).
[77] Y. Perez-Riverol, et al., The PRIDE database resources in 2022: a hub for mass spectrometry-based proteomics evidences, Nucleic Acids Res. 50 (2022) D543–D552.